Full length article

Sandwich assemblies of composites square hollow sections and thin-walled panels in compression

Xie Lei[a], Qi Yujun[b,**], Bai Yu[a,*], Qiu Chengyu[a], Wang Hao[c], Fang Hai[b], Xiao-Ling Zhao[d]

[a] *Department of Civil Engineering, Monash University, Clayton, Victoria, 3800, Australia*
[b] *College of Civil Engineering, Nanjing Tech University, Nanjing, 211800, China*
[c] *Centre for Future Materials, University of Southern Queensland, Toowoomba, QLD, 4350, Australia*
[d] *Department of Civil and Environmental Engineering, The University of New South Wales (UNSW), Sydney, NSW, 2052, Australia*

ABSTRACT

Sandwich structures were built up by two glass fibre reinforced polymer (GFRP) thin-walled panels and square hollow sections (SHS) in between through adhesive bonding or mechanical bolting. Experiments in compression were conducted in order to understand the failure modes including global and local buckling, load-bearing capacities, load-displacement curves and load-strain responses. Accordingly the effects of different connection methods and different spacing values between the SHS sections were clarified. Sudden debonding failure between GFRP panels and inner SHS columns was found on adhesively bonded specimens; while mechanically bolted specimens showed evident lateral deformation and progressive failure until the ultimate junction separation failure on the GFRP SHS columns. Local buckling was found on GFRP thin-walled panels of specimens with a larger spacing between the two SHS sections. Finite element analysis and analytical modelling were performed to estimate the load-displacement curves and the critical stress for the local buckling on GFRP thin-walled panels, where consistent agreements with experimental results were received.

1. Introduction

Sandwich structures generally consist of two facesheets and a core where the facesheets can be made of glass fibre reinforced polymer (GFRP) composites and the core can be lightweight materials such as polymer foams and natural woods [1,2]. Such sandwich structures with GFRP composites are featured with light weight and satisfactory mechanical performance, and therefore presenting successful structural applications in many fields such as aerospace, aeronautical and marine industries [3]. In civil engineering applications, such sandwich structures [4–6] have attracted increasing interests in structural applications especially in modular buildings [7], e.g. beams [8–12], floors [13,14], cladding [15,16] and bridge decks [17–20].

Numerous studies were conducted for GFRP sandwich structures under bending [8–12,18,20], the work to investigate of their behaviour under compression for column or wall applications are relatively limited although it is understood that GFRP composites may be more critical in compression due to low elastic modulus and shear strength [21,22]. The compressive behaviours of GFRP wall panels in sandwich

structures using glass/polypropylene(PP) composites as the facesheet and polystyrene(PS) foam as the core were examined by Mousa and Uddin [23,24]. Concentric and eccentric compression experiments were carried out on such sandwich structures for application of wall panels; and debonding between the facesheets and core was found as the main failure mode for such sandwich wall panels under compression. Furthermore, experimental results including the global buckling loads, lateral deflections and wrinkling stress were analysed and analytical formulations and finite element (FE) analysis were well validated accordingly. Slender sandwich panels with different rib configurations using GFRP laminates as facesheets and polyurethane (PU) foam as the core were developed by Mathieson and Fam [25] and experimental and numerical work was conducted to investigate their performance under axial compression. The effects of slenderness ratio on the failure modes and load-bearing capacities of such sandwich wall panels were analysed and clarified in Ref. [26]. Another sandwich wall panels using hand lay-up GFRP as facesheets and PU foam as the core were developed by Abdolpour et al. [27]. Experiments were performed to study the mechanical performance of two scenarios: single sandwich unit and

jointed sandwich units. It is found that the global buckling and GFRP local wrinkling are the dominant failure modes and further the axial load capacities of single and joint wall panels can be evaluated using proposed analytical formulas. The effects of foam density and slenderness ratios were examined by CoDyre and Fam [28] to understand the compressive strength of sandwich panels made of GFRP facesheets and polyisocyanurate foam core. Other studies on circular sandwich columns made of GFRP fabrics (as facesheets) and different cores including polyvinyl chloride (PVC) foam [29] or PU foam [30] are also conducted for structural applications.

One of the typical connection methods to build a sandwich structure using composites is adhesive bonding, which bonds the two facesheets and the core together [31–33]. Alternatively, mechanical bolting [34] has been used to form various GFRP structures including sandwich assemblies as reported in Refs. [35–39]. In comparing to adhesive bonding, mechanical bolting has characteristics of easy assembly and disassembly [40] and quasi-ductile behaviour [41]; while may be associated with higher stress concentration [42–45] at the bolted region. GFRP web-flange sandwich structures were developed using standard and blind bolts by Satasivam and Bai [46] and experimentally examined four point bending. It was shown that such GFRP web-flange sandwich structures [14,46], also known as multi-cellular structures [47], have improved flexural stiffness over individual GFRP sections and been used for bridge deck and building floor applications [48,49]. However, studies on such web-flange sandwich structures formed with adhesive bonding or mechanical bolting under compression are still needed especially for their potential column or wall applications.

This paper presents an experimental investigation on the axial compressive performance of GFRP sandwich assemblies with bonded or bolted connections. GFRP sandwich wall specimens were fabricated by two pultruded GFRP flat panels as face sheets sandwiching square hollow sections (SHS) using adhesive bonding or mechanical bolting. Experimental results on the failure modes, load-bearing capacities, load-displacement curves and load-strain responses were obtained and compared with numerical and theoretical modelling. The effects of connection types (adhesive bonding or mechanical bolting) and spacing between the core SHS sections on the overall load-bearing capacities and failure modes are discussed. Finite element (FE) analysis was also carried out to validate the experimental results in terms of the load-displacement curves with consideration of second order effects.

2. Experimental investigation

2.1. Materials

Pultruded GFRP flat panels and square hollow sections (SHS) are used in this study to fabricate sandwich specimens. The nominal length of the used GFRP flat panels and SHS columns are 3000 mm to present the full scale for one-story column or wall applications. The nominal thickness of GFRP flat panels is 8 mm and the section dimension of GFRP SHS is $102 \times 102 \times 9.5$ mm. Pultruded GFRP materials have unidirectional fibres in the longitudinal direction and are regarded as an orthotropic material. The material properties of used pultruded GFRP flat panels and SHS columns in the longitudinal and transverse directions were determined by coupon tests. Tensile properties of GFRP flat panels were determined as the average of five coupon specimens in accordance with ASTM D3039. The material properties of GFRP SHS in the longitudinal direction were determined through 100 mm height short column compression tests [50]. All the resulting properties are summarized in Table 1, where the elastic modulus of GFRP panels in the longitudinal direction (fibre orientation) and transverse direction is 30.5 GPa and 9.5 GPa, respectively; and the elastic modulus of GFRP SHS in the longitudinal direction is 28.1 GPa.

Table 1
Material properties of pultruded GFRP materials.

	Direction	Elastic modulus (GPa)	Ultimate strength (MPa)
Face sheet	Longitudinal	30.5	387.9
	Transverse	9.5	59.3
SHS	Longitudinal	28.1	220.7

2.2. Specimens

Four GFRP sandwich specimens were prepared and experimentally studied. Those specimens were assembled by connecting two pultruded GFRP panels (as facesheets) and two pultruded GFRP SHS columns (as core) in between. Two different connection methods, i.e. adhesive bonding and mechanical bolting, are employed to assembly those sandwich specimens. Specimens are labelled based on their connection methods, e.g. "AB" represents adhesive bonding, and "MB" represents mechanical bolting. The configuration of those sandwich specimens after assembly is presented in Fig. 1. The spacing (*c*) between two SHS sections is an experimental parameter to investigate its effect on the mechanical performance of the sandwich specimens, with consideration of two spacing values of 96 and 246 mm. The nominal height of all specimens is 3000 mm, and the detailed dimensions of all specimens are measured and summarized in Table 2.

For all sandwich specimens, the longitudinal direction is the pultrusion fibre orientation, corresponding to the material properties provided in Table 1. AB series specimens were assembled using Plexus MA310, a two-part methacrylate adhesive with the nominal glue thickness of 0.6 mm. This adhesive has a tensile strength range of 24.1–31.0 MPa, a tensile modulus range of 1.0–1.2 GPa, and a shear strength of 20.7–24.1 MPa [51]. The surfaces of GFRP panels and SHS columns were firstly roughed using angle grinders and then cleaned using acetone solvent. After that, part A and B of MA310 adhesive were mixed together at the weight ratio of 1:1. The mixed MA310 adhesive was applied on one GFRP panel, and two SHS columns were bonded on the GFRP panel according to the geometric spacing defined in Table 2. To maintain consistent thickness of the adhesive layer, chopped steel wires with the diameter of 0.6 mm were used as spacer at the interfaces of GFRP SHS and face sheets. Heavy steel blocks were placed on the SHS columns to ensure the full contact of adhesive between the SHS columns and panels. The adhesive was cured at room temperature for 72 h. After that, the specimen was flipped and the GFRP panel on the other side was bonded to the inner SHS columns following the same procedures. MB series specimens were assembled by tightening M10 bolts (class 10.9) through the central line of the GFRP SHS section, as shown in Fig. 1. The pitch between each bolt row is 100 mm. The overall length of the used M10 bolts is 150 mm, and the thread length is 35 mm. The nominal tensile strength of the bolts is 1000 MPa. The nominal diameter is 12.5 mm for of all bolt holes, and the nominal clearance distances are 51 mm (to the side edge) and 100 mm (to the end edge). For each MB series specimen, in total 58 through bolts are used for assembly.

2.3. Setup and instrumentation

Testing machine (YAW-10000 J) with a loading capacity of 10,000 kN is used to apply the compression loading on the GFRP sandwich specimens. The overall setup is shown in Fig. 2(a) and (b). The bottom end of the specimen sat on the steel base ground between two pieces of steel angles and was fixed by tightening using two through bolts. One side of each steel angle was welded on the steel base ground to ensure no displacement and rotation there. For the top end setup, the two pieces of steel angles were mounted by bolts to the
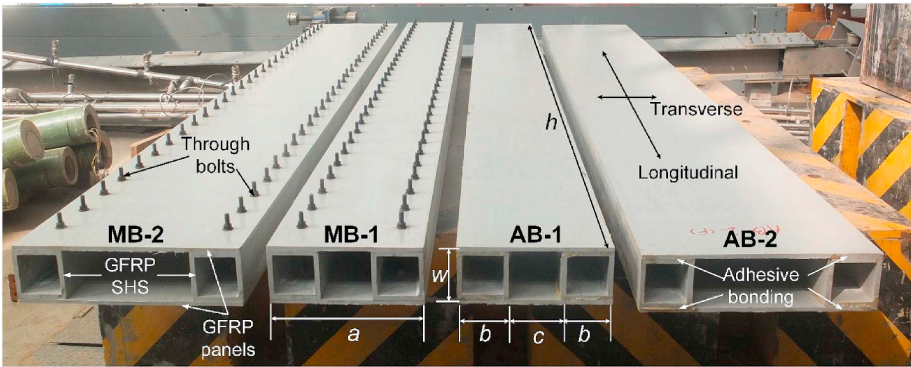
Fig. 1. Configurations of GFRP sandwich specimens.

Table 2
Dimensions of GFRP sandwich specimens.

Specimen	a	c	w	h	T_c	T_p
AB-1	299.6	97.5	117.6	3005	10.3 ± 0.3	7.9 ± 0.2
AB-2	450.6	249.7	117.9	3005	10.2 ± 0.5	8.0 ± 0.3
MB-1	301.3	98.8	116.5	3005	10.2 ± 0.4	7.8 ± 0.3
MB-2	451.5	250.6	116.3	3005	10.1 ± 0.5	7.9 ± 0.2

Note: a = specimen width; c = spacing between SHS sections; w = specimen depth; h = specimen height; T_c = thickness of SHS sections; T_p = thickness of panels.
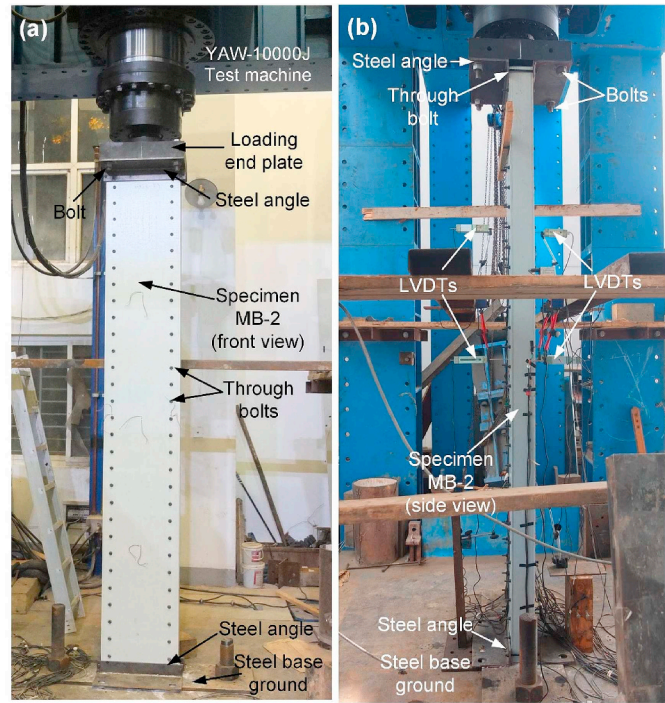

Fig. 2. Experimental setup: (a) front view; (b) side view.

loading end plate (see Fig. 2(a)). The top loading plate of the loading machine has a sphere inside, resulting in the pinned boundary condition for the top end.

The compressive loading rate was 1 mm/min in a displacement control mode for all specimens. The axial shortening displacement is measured by a linear variable displacement transducer (LVDT) installed at the central axis of the top loading plate. Lateral displacements on both front and back sides of the specimens are measured at the positions of 1/4, 1/2 and 3/4 height of the specimens as illustrated in Fig. 3. Strain gauges were adhered along the central line of specimens at 1/4,
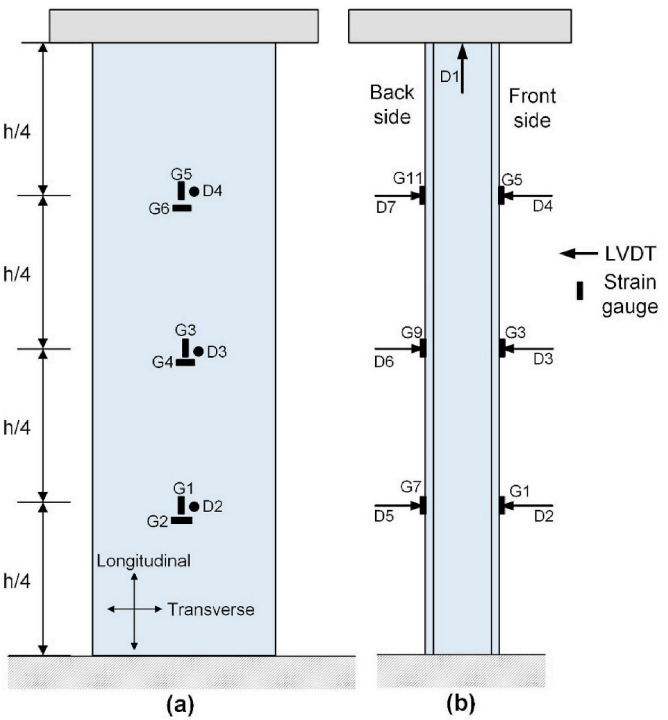

Fig. 3. Experimental instrumentation: (a) Front view; (b) Side view.

1/2 and 3/4 height on both the front and back sides, as shown in Fig. 3. At each height position, strain gauges are placed in both longitudinal and transverse directions. In total 12 strain gauges are used for each specimen. During the experiments, failure modes were monitored and recorded by several video cameras in the laboratory.

3. Finite element analysis

Finite element (FE) analysis was performed to evaluate the mechanical performance of GFRP sandwich specimens using software ANSYS 15.0. Both GFRP SHS and panels were modelled using element SOLID45 which is an 8-node 3D solid structural element with three translational degrees of freedom. Element size was set as 20 mm to receive fine meshing results for these GFRP components. The material properties used in FE modelling were defined according to the experimentally acquired values listed in Table 1.

Fig. 4(a) show the cross-section of AB specimens, in which the adhesive bonding between the inner GFRP SHS sections and outer GFRP panels were also modelled using SOLID45 elements and the thickness was set as 0.6 mm. The bonding between GFRP panels and SHS sections was achieved by node coupling method, i.e. the coincident nodes
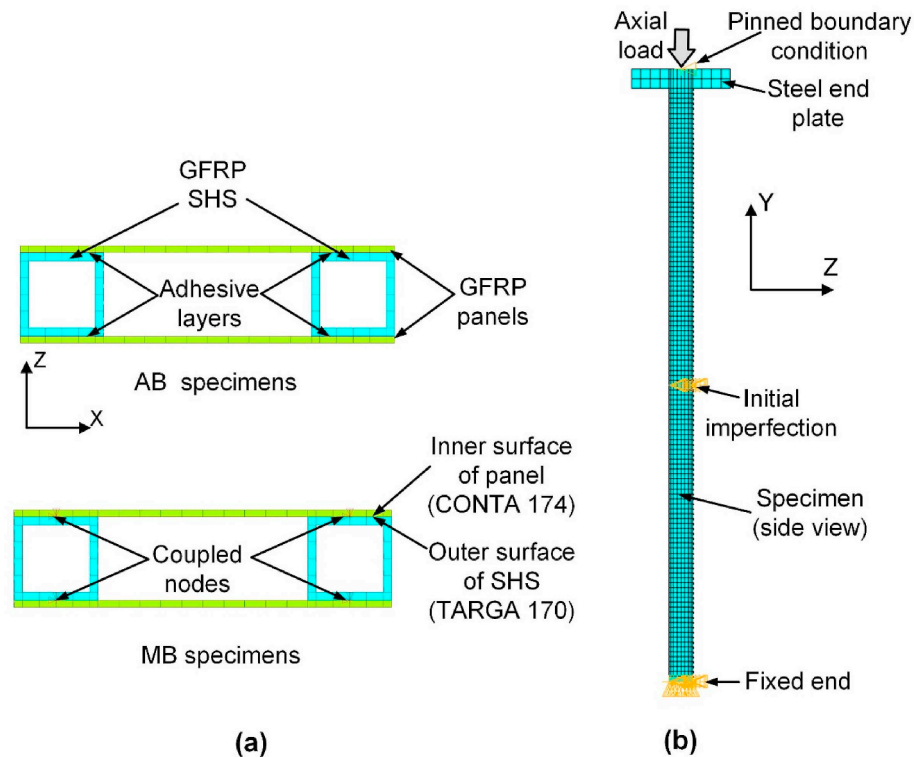
Fig. 4. FE modelling with (a) cross-sectional views of AB and MB specimens.

between adhesive layers and GFRP panels/SHS sections were coupled for all degrees of freedom. For MB specimens assembled using through bolts, the bolted connection was modelled by coupling the coincident nodes only at the bolted regions between the GFRP SHS sections and GFRP panels, as shown in Fig. 4(a). For each bolt position, the coincident nodes were coupled for all degrees of freedom. All the contact areas of MB specimens between the outer surface areas of the GFRP SHS sections and the corresponding inner areas of the GFRP panels were modelled using a pair of contact elements, i.e. Conta174 and Targa170. As shown in Fig. 4(a) for MB specimens, the outer surface areas of the two GFRP SHS was defined as target element Targa170, and the inner surface areas of GFRP panels was defined as contact element Conta174. This contact behavior allows free separation in the normal direction but defines the contact stiffness as the surface material with consideration of minor penetration (10% of the depth of the underlying element Conta174 [52]). In the tangent direction, the friction coefficient was set as 0.42 [53].

Regarding the boundary conditions, all the nodes on the bottom end of the specimens were constrained for all degrees of freedoms to represent the fixed boundary condition as shown in Fig. 4(b). For the top end, a steel plate with dimensions of $500 \times 500 \times 50$ mm was modelled for the actual loading plate during the experiments. The coincident nodes at the interface between the steel loading plate and the top end of the GFRP sandwich specimen were coupled as well to simulate the constraining effects of the steel angles. The translational degrees of freedom of the nodes in the central line of the top end of the steel plate were restrained in X and Z directions, leaving Y direction free for rotation to represent the pinned boundary condition for the top end, as shown in Fig. 4(b).

An initial lateral deflection of 1/500 of the specimen height in the Z direction was defined in the middle section of the specimen as the initial imperfection to introduce geometric nonlinearity. After that, axial displacement loading was applied on the nodes of the central line of the top end on the steel plate and geometric non-linear analysis was further performed.

4. Experimental results

4.1. Failure modes

Detailed observations on the failure modes and progressions of each specimen were made during the experiments. For Specimen AB-1, at the early stage of loading, adhesive bond cracking sounds were heard occasionally after the load increased to above 300 kN. No obvious lateral deformation was visually observed to indicate overall buckling. When the axial load reached around 1075 kN, a sudden loud sound were heard due to the separation of the panel on the back side from the inner SHS columns as shown in Fig. 5. The face sheet on the back side was severely buckled, but the inner SHS columns and the face sheet on the front side remained without noticeable buckling as no obvious lateral deformations were observed. Observation on the debonding area indicated that the debonding started from the middle of the specimen and extended to the ends (see Fig. 5). On the tip region of both ends, it was found that some adhesive was still in contact and not debonded. After the separation between the back face sheet and inner SHS sections, the sandwich specimen is considered as entirely failed and the experiment was stopped.

For specimen AB-2, the failure progression was similar to AB-1. With the increase in loading, adhesive cracking sounds were heard after the load became over 400 kN. The ultimate debonding failure occurred when the axial load reached 1038 kN, with a loud sound. As shown in Fig. 6, for this specimen both the front and back face sheets were severely buckled and separated with the inner SHS components. Again there was no obvious lateral deformation observed on the SHS components; and the experiment was stopped after the ultimate debonding failure.

For specimen MB-1, with the increase in the loading, overall buckling was visually observed in the early loading step (see Fig. 7(a)) and the lateral deformation continued increasing afterwards. When the axial load was approaching the peak load (1126 kN), several cracking sounds were heard while no cracking due to buckling was visually
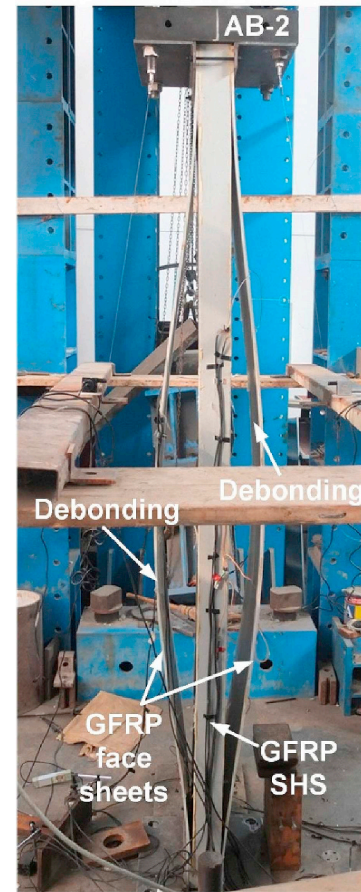
Fig. 5. Failure mode of specimen AB-1.

Fig. 6. Failure mode of specimen AB-2.

Fig. 7. Failure modes of specimen MB-1: (a) global buckling initiation; (b) side view of end crushing; (c) cross-sectional view of end crushing.

observed from the specimen surface. After the peak load, the load slightly dropped to 1082 kN and end crushing in association with the delamination of the back side GFRP face sheet (under compression) and the junction separation of SHS column were observed, as shown in Fig. 7(b) and (c). After this failure, the axial load dropped substantially and the experiment was stopped thereafter.

Overall buckling initiation and increasing lateral deformation were also observed for specimen MB-2 at early loading stage. When the axial load reached 977 kN, wrinkling was found from the 1/3 height region (between 10th and 11th rows of bolts) of the back face sheet (see Fig. 8(a)), and the load dropped substantially to 780 kN. After that, the axial load continued to increase. At the load of 1048 kN, wrinkling was also found from the upper region (around at the height of 2.7 m, see Fig. 8(b)) of the front face sheet. The load then continued to increase and the ultimate failure was found from the back face sheet around at the height of 1.2 m, see Fig. 8(c), where both face sheet wrinkling and also junction separation of the SHS sections occurred and this time this specimen lost its load capacity. It should be noted that no bending or shear failure on the through bolts were found. At the regions where the ultimate junction separation of GFRP SHSs occurred, several longitudinal and transverse dents on the GFRP face sheet were found near the bolt hole regions as shown in Fig. 8(d) likely due to the local effects of bolting.

4.2. Load-axial displacement curves

Fig. 9 presents the load-axial displacement relationships for all specimens. It shows that for AB specimens, the load-displacement curves are highly linear until a sudden drop when the ultimate failure (debonding) occurs. For specimen MB-1, it has a slight drop at a peak load of 1126 kN, and keep carrying the loading until the ultimate failure (see Fig. 9) at load 1082 kN. For specimen MB-2, three load
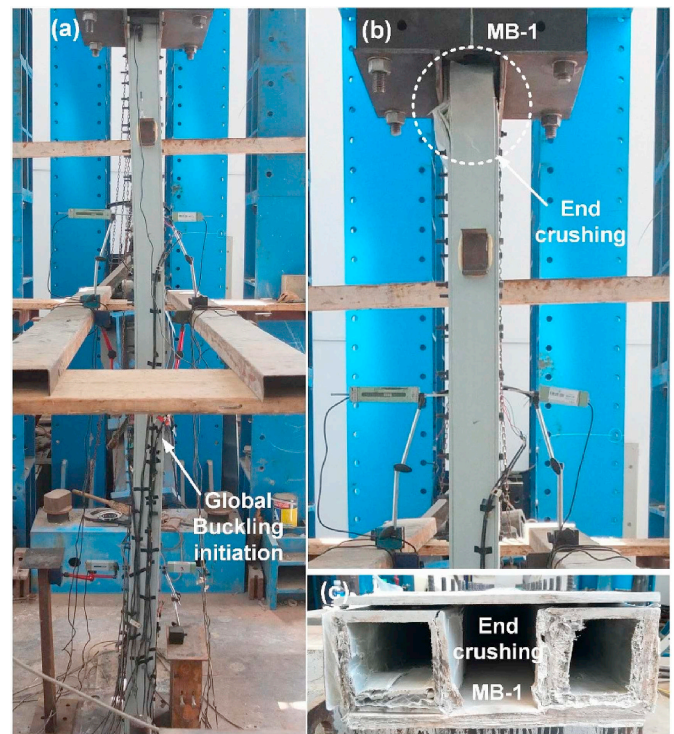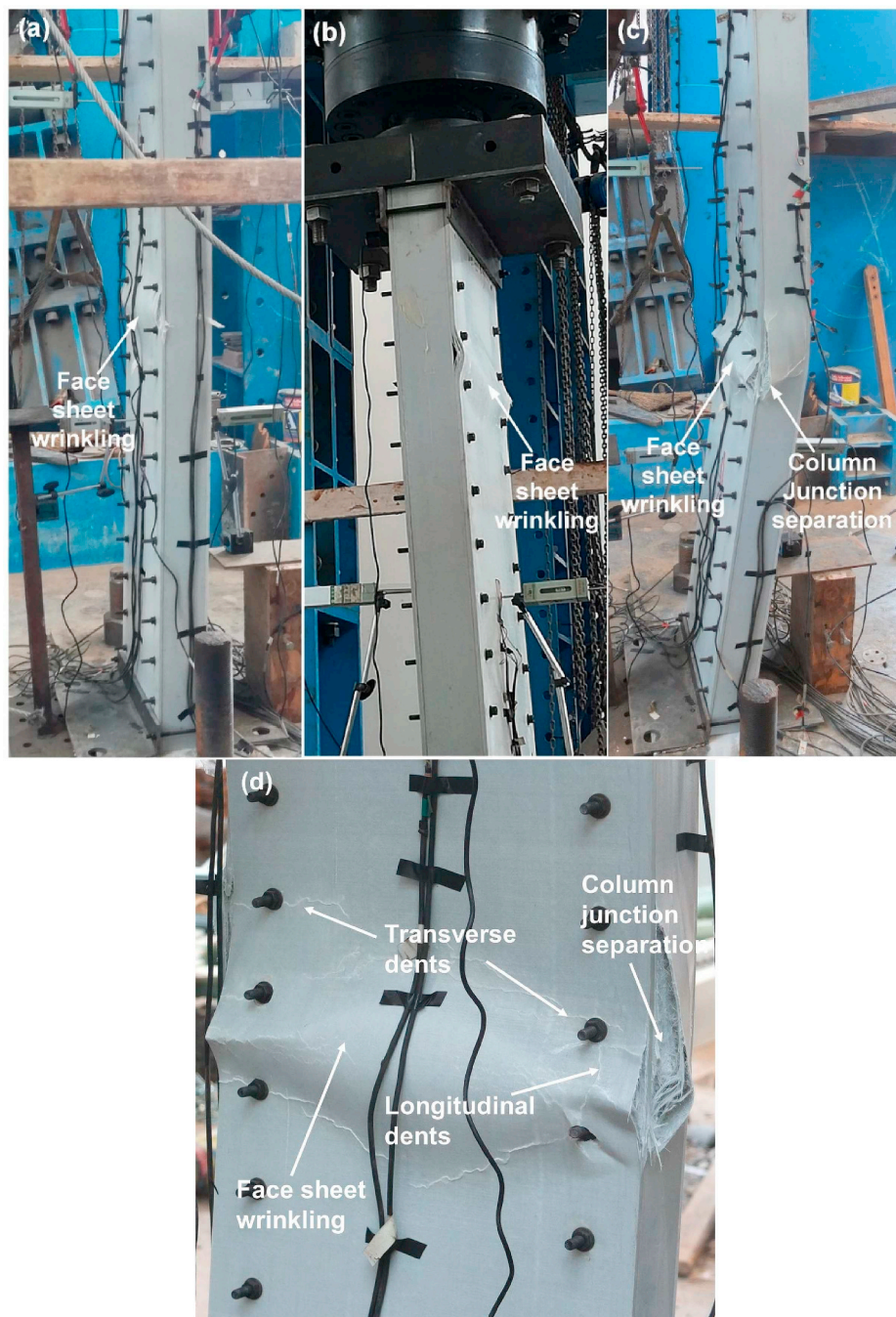
Fig. 8. Failure modes of specimen MB-2: (a) back face sheet wrinkling; (b) front face sheet wrinkling; (c) further back face sheet wrinkling and column junction separation; (d) longitudinal and transverse local damages near bolt hole regions.

drops can be seen corresponding to the face sheet wrinkling observed in Fig. 8. Based on the comparison of the load-axial displacement curves of specimens with the same sectional width (AB-1 and MB-1, or AB-2 and MB-2), it is found that AB specimens have a slightly higher stiffness (slope of the curves) than MB specimens. This may be due to the composite action offered by different connection approaches. Adhesive bonding is considered with full composite action [14] while the mechanical bolting with partial composite action depending on the number and spacings of the mechanical bolts and their mechanical properties etc [46]. Also, the difference of effective widths between AB and MB specimens may lead to the difference in the axial stiffness. As further presented in Table 4 and Fig. 15, for the specimens with the same width but different connection method, AB specimens have a

shorter effective width comparing to MB specimens; this further results in a higher critical local buckling stress for the face sheets and also a higher axial stiffness of the specimen. Ultimate axial displacements of each specimen at its ultimate load are summarized in Table 3. The ultimate displacements of specimen AB-1 and AB-2 are 11.4 mm and 9.7 mm and they are less than the corresponding values of specimens MB-1 (15.2 mm) and MB-2 (14.9 mm). It is understandable as the AB specimens experienced sudden debonding failure without the global buckling initiation while MB specimens showed progressive failure after the global buckling initiation.

FE modeling results are included in Fig. 9 to compare with the experimental results. Overall, the load-displacement curves from FE analysis showed good agreement with the experimental results
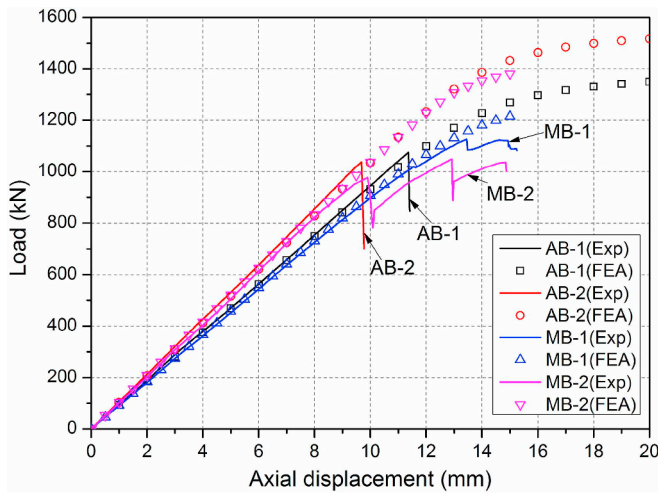
Fig. 9. Load and axial displacement curves for all specimens from both experiments and FE modelling.

especially for the linear developments at the initial stages. It should be noted that the FE results did not well describe the load-displacement behaviours for MB specimens after wrinkling of face sheets as such failure mode were not considered in the FE modelling.

4.3. Load-lateral displacement curves

The load-lateral displacement curves are presented in Fig. 10. LVDT results measured from the 1/4 (D2 and D5), 1/2 (D3 and D6) and 3/4 (D4 and D7) height positions on both front and back sides of each specimen at the ultimate loads are summarized in Table 3. For specimen AB-1, the readings from D2, D3, D4 on the front side are negative values and D5, D6, D7 on the back side are positive values, suggesting that the specimen is under an overall lateral deformation towards to the front side. Prior to the adhesive debonding occurred on the back side at the axial load of 1075 kN, the largest lateral displacements from LVDTs D3 and D6 in the middle of the specimen are only 7.6 mm and 8.1 mm (see Table 3) respectively. After the sudden adhesive debonding failure, the lateral displacements D5, D6 and D7 on the back side panels increased substantially. The lateral deformations on specimen AB-2 are similar to AB-1. All the readings are relatively small (less than 6 mm) until the adhesive debonding failure occurred at ultimate load of 1038 kN. After the sudden adhesive debonding failure, all the lateral displacements increased substantially. It should be noted that from the lateral displacements of AB series specimens are low before the ultimate failure as evidenced in Fig. 10(a) and (b), suggesting insignificant global buckling.

For MB specimens, the load-lateral displacement curves presented in Fig. 10(c) and (d) show that lateral displacements developed continuously with relatively large values, unlike the sudden increase in AB series specimens. The largest lateral displacement readings before failure (D3 or D6, see Table 3) at the middle height of GFRP face sheets

are 45.0 mm or 47.6 mm from specimen MB-1, and 49.3 mm or 42.2 mm from specimen MB-2. These large lateral deformations on MB series specimens made the bucked deformation visible during the experiments, and further suggesting that the global buckling may be initiated for the specimens.

4.4. Load-strain responses

The load-strain responses of each specimen are presented from Figs. 11–14, with the corresponding positions of strain gauges marked in Fig. 3. On the front side of the specimens, strain gauges G1, G3, G5 represent the longitudinal strains on the 1/4, 1/2 and 3/4 height positions; and G2, G4, G6 correspond to the transverse strains on the same positions. On the back side of the specimens, strain gauges G7, G9, G11 represent the longitudinal strains on the 1/4, 1/2 and 3/4 height position; and G8, G10, G12 correspond to the transverse strains on the same positions. Fig. 11 presents the load-strain responses on specimen AB-1, where both longitudinal and transverse strain responses appear linear. It is also shown that the slopes of longitudinal strains (G7, G9, G11) on the back side are higher than those (G1, G3, G5) on the front side. This is because the overall lateral deformation of the specimen as presented in Fig. 10(a), in addition to the axial loading, caused the different compression on the front and back sides. The maximum compressive strain is -0.37% on G3 gauge located on the middle height of the front face sheet at the ultimate load of 1075 kN. The maximum transverse strain is 0.11% on G2 located on the 1/4 height position of the front face sheet at the ultimate load.

Fig. 12 presents the load-strain responses of specimen AB-2. Again at the initial loading stage all the strain responses are linear. However different to specimen AB-1, the transverse strain from G8 showed a clear turning of direction after the compressive load of about 900 kN. This sudden change of strain values indicates that local deformation (buckling) at this location of the GFRP face sheet. The longitudinal strain development from G7 (on the same position of G8) also show change in slope, in support of the observation of the local buckling behaviour. The maximum compressive strain at the ultimate load of 1038 kN is -0.27% on gauge G9 located on the middle of the back side; and the maximum transverse strain is 0.08% on G10 located on the middle height position on the front side.

Fig. 13 presents the load-strain responses of specimen MB-1. When the compressive load increased over 1000 kN, strain behaviours from G3, G5, G9, G11 on the 1/2 and 3/4 height positions gradually changed their development trends. This suggests the overall bending because of the initiation of global buckling and this is in accordance with the observed lateral deformation as shown in Figs. 7(a) and Fig. 10(c). Fig. 14 presents the load-strain responses of specimen MB-2 where more obvious change in the strain developments with loading are found. Clear turning points in the responses from gauges G7, G8 and G9 at load of 750 kN indicated local buckling occurred on the 1/4 and 1/2 height on the back face sheet. Although this local buckling was not observed visually during experiment, this region where the local buckling occurred was in general consistent with the further observed face sheet wrinkling (see Fig. 8(a)) on the lower area of the back face sheet. Other changes in the direction of strain developments are from gauges G7, G9

Table 3
Major experimental results of GFRP sandwich specimens.

Specimen	Peak load P (kN)	Ultimate load P_u (kN)	Axial displacement at P_u (mm)	Lateral displacement at P_u (mm) (Front side)			Lateral displacement at P_u (mm) (Back side)		
				D2	D3	D4	D5	D6	D7
AB-1	1075	1075	11.4	3.0	7.6	4.5	3.7	8.1	3.6
AB-2	1038	1038	9.7	5.1	5.2	3.3	2.3	5.7	4.9
MB-1	1126	1082	15.2	17.4	45.0	30.6	22.1	47.6	33.3
MB-2	1048	1001	14.9	32.7	49.3	25.8	20.9	42.2	15.5

Table 4
Comparisons between analytical and experimental results of ultimate compressive stress.

Specimen	b_{eff} (mm)	Analytical results (MPa)		Experimental results (MPa)		Comparisons		
		σ_e	σ_{LB}	σ_u	$\sigma_{LB,exp}$	σ_u/σ_e	σ_u/σ_{LB}	$\sigma_{LB,exp}/\sigma_{LB}$
AB-1	96	110.0	552.1	88.2	/	0.80	0.16	/
AB-2	246	114.8	81.5	70.3	60.9	0.61	0.86	0.75
MB-1	196	109.9	149.8	94.9	/	0.86	0.63	/
MB-2	346	114.8	48.1	73.6	52.7	0.64	1.53	1.10

Note: b_{eff} = effective plate width; σ_e = global buckling stress; σ_{LB} = local buckling stress; σ_u = experimental ultimate compressive stress; $\sigma_{LB,exp}$ = experimental local buckling stress.

and G10 at the load of 830 kN, further confirming the occurrence of local buckling there on the back face sheet.

5. Discussions

5.1. Load-bearing capacity

The global buckling load of the sandwich specimens can be estimated using Eq. (1):

$$P_E = \frac{\pi^2 (EI)_{eq}}{(kL)^2} \tag{1}$$

where $(EI)_{eq}$ is the equivalent flexural stiffness of the section, k is the effective length ratio and L is the length of the specimen.
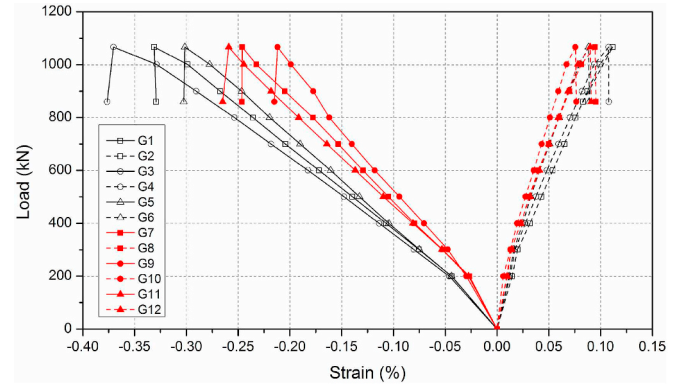
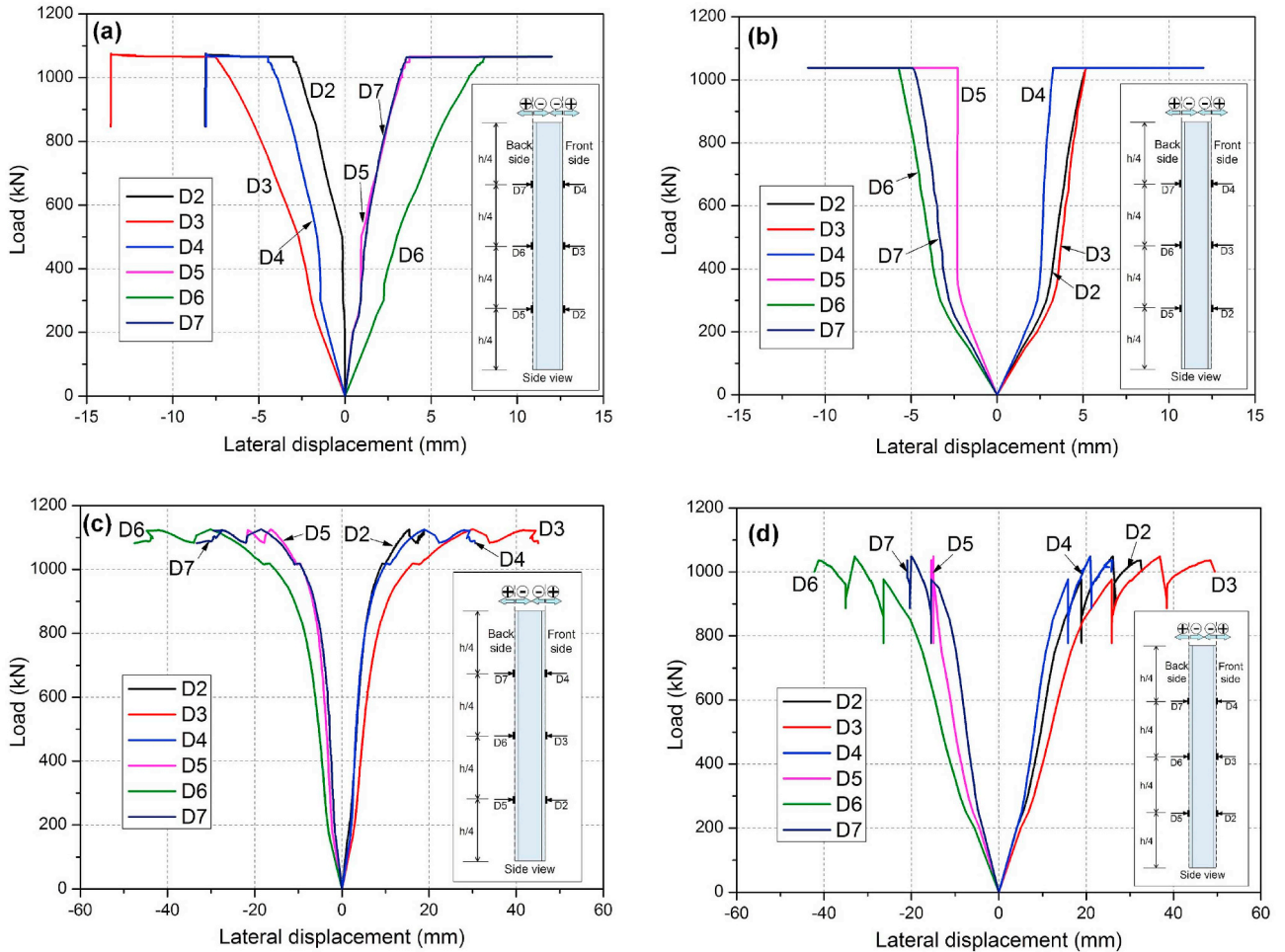**Fig. 11.** Load-strain responses of specimen AB-1.

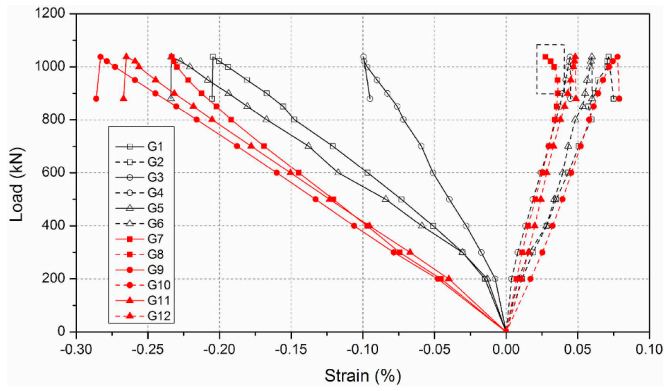**Fig. 10.** Load and lateral displacement curves: (a) AB-1; (b) AB-2; (c) MB-1; (d) MB-2.
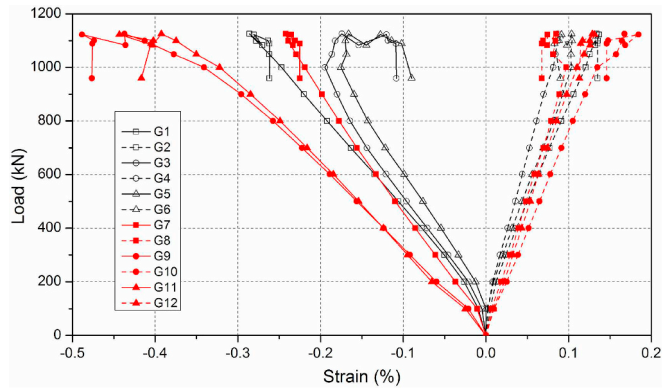
Fig. 12. Load-strain responses of specimen AB-2.
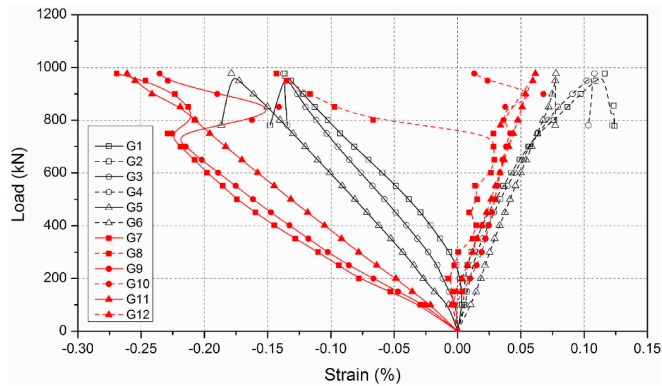

Fig. 13. Load-strain responses of specimen MB-1.

Fig. 14. Load-strain responses of specimen MB-2.

Fig. 15. Boundary conditions for GFRP face sheets in theoretical estimation of local buckling stress: (a) cross-sectional view; (b) front view.

for the connection between the GFRP face sheets and inner SHS sections. However, only the bonded connection may provide full composite action [49]; while partial composite action was found on bolting connected web-flange sandwich systems [46]. The critical global buckling stress of all sandwich specimens are calculated using Eq. (1) and summarized in Table 4 for further comparison. It also can be found that the critical global buckling stress of MB specimens are overestimated indicating the partial composite action for the sandwich specimens with bolted connections.

For specimens AB-2 and MB-2 with a larger spacing c (246 mm) between the two SHS sections, local buckling may more likely occur on the GFRP face sheets between the two SHS sections, due to the relative high width-thickness ratios [50,54]. The critical local buckling load can be calculated, taking into consideration the boundary conditions of the GFRP face sheets of the AB or MB specimens with different connections. For the former, the boundary condition of the GFRP face sheets may be close to simple supported at the top and bottom edges while as clamped due to the adhesive bonding at the two sides, i.e. CCSS as shown in Fig. 15. The equivalent plate width is therefore the clear spacing between the two SHS sections. The critical local buckling load for orthotropic GFRP plate with boundary condition of CCSS [55–57] can be calculated using the below equation:

$$N_{Local,cr}^{CCSS} = \frac{\pi^2}{b_{eff}}\left[\frac{44.9}{\pi^2}\sqrt{D_{11}D_{22}} + \frac{24}{\pi^2}(D_{12} + 2D_{66})\right]$$

$$(3)$$

where b_{eff} is the width of the plate, and D_{11}, D_{22}, D_{12}, D_{66} are the bending stiffness coefficients of the plate relating to material properties [57,58]. Eq. (3) was further used for MB series specimens. However the effective plate width b_{eff} may be considered as the distance between the two through bolts in the two SHS sections from the same row (as indicated in Fig. 15). Using Eq. (3), the critical local buckling stress of AB and MB series specimens are calculated and summarized in Table 4.

In Table 4, the experimental ultimate compressive stress σ_u of specimens AB-1 and AB-2 are 88.2 MPa and 70.3 MPa, corresponding to the stress ratio of 0.80 and 0.61 to the calculated global buckling stress

In this study, the boundary condition on the ends corresponds to one end pinned and the other fixed, therefore k is 0.7. The equivalent flexural stiffness of the section can be calculated using the below equation:

$$(EI)_{eq} = (EI)_{panels} + (EI)_{SHS} = 2E_p\left(\frac{b_p t_p^3}{12} + b_p t_p d^2\right)$$

$$+ 2E_c\left[\frac{b_c^4}{12} - \frac{(b_c - t_c)^4}{12}\right]$$

$$(2)$$

where E_p and E_c are the elastic moduli of GFRP panels and SHS columns, b_p and t_p are the width and thickness of GFRP panels, and b_c and t_c are the width and thickness of GFRP SHS sections; d is the distance between the central axis of the SHS sections and the central axis of the GFRP panels, i.e. $(b_c + t_p)/2$.

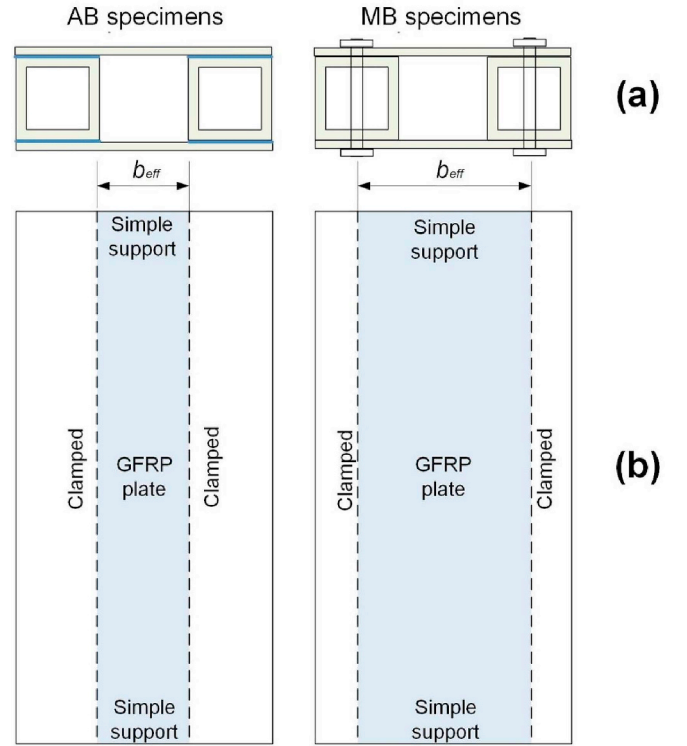It should be noted that full composite action is assumed in Eq. (2)

σ_e. This is in support of the observed failure mode of AB series specimens, i.e. sudden debonding without global buckling. For MB specimens, the experimental ultimate compressive stress σ_u are 94.9 MPa and 73.6 MPa, corresponding to the stress ratio of 0.86 and 0.64 to the global buckling stress σ_e; while the calculated values can be overestimated because of the assumption of full composite action as discussed above. In addition, for specimen MB-1, the stress ratio 0.86 can already reasonably suggest the global buckling initiation, as observed during the experiment (Fig. 7(a)). For specimen MB-2, the stress ratio is 0.64 and much lower than the theoretical global buckling stress. This is due to the occurrence of local buckling on MB-2 specimen associated with a larger width between the two through bolts from the same row (see Fig. 8(a) and b). The calculated local buckling stress σ_{LB} is 48.1 MPa and less than the calculated global buckling stress σ_e for specimen MB-2.

The comparisons of local buckling stress between the calculated and experimental values in Table 4 show satisfactory agreements for specimens AB-2 and MB-2. For these two specimens AB-2 and MB-2 with a larger spacing between the two SHS sections, the calculated local buckling stress σ_{LB} are 81.5 MPa and 48.1 MPa, and lower than the global buckling stress σ_e. σ_{LB} of specimen MB-2 is close to the experimental local buckling stress $\sigma_{LB,exp}$ of 52.7 MPa and local buckling was evidently observed from the failure mode (face sheet wrinkling, see Fig. 8(a) and b) and from several load-strain responses (G7, G8, G9 and G10 in Fig. 14). For specimen AB-2, the ratio of local buckling stress between experimental and theoretical results is 0.75. This may be due to the approximation of boundary conditions of GFRP face sheets in specimen AB-2. The boundary conditions of two sides in the longitudinal directions were considered as clamped. However, the constrains from the adhesive bonding and the thin thickness of the face sheets may still allow rotation at the side ends. This may result in overestimation of the critical theoretical local buckling stress σ_{LB} in Eq. (3). On the other hand, theoretical calculations on the local buckling stress σ_{LB} for specimens AB-1 and MB-1 are 552.1 MPa and 149.8 MPa and they are higher than their experimental ultimate compressive stress σ_u as well as the theoretical global buckling stress σ_e. This explains that there is no local buckling observed from these two specimens.

5.2. Effects of spacing between SHS sections

As evidenced in load-strain responses presented in Figs. 11–14, the spacing value c shows clear effect on the local buckling of the GFRP face sheets between the two SHS sections. Specimens with a larger spacing value (AB-2 and MB-2) exhibited local buckling mode (as shown in Figs. 12 and 14); while the ones with a smaller spacing (AB-1 and MB-1) did not (see Figs. 11 and 13). Also the actual spacing between the two clamped side edges in MB specimens is larger than that between the two SHS sections due to the inner positions of bolts. It also modified the boundary conditions and therefore affected the critical local buckling stress for the GFRP face sheets between the two bolts as discussed previously. In the development of such GFRP sandwich assemblies for column or wall applications, the spacing between SHS sections should be carefully determined as it affects the failure mode and overall load-bearing capacities.

5.3. Comparison of bonded and bolted connections

From the observed failure modes, adhesively bonded specimens AB-1/2 exhibited sudden debonding. The bolted specimens MB-1/2 exhibited progressive failure associated with the evident global buckling initiation, and finally failed on the junction separation on the inner SHS sections. From the load-axial displacement curves, AB specimens showed a slightly higher axial stiffness than MB specimens. This reflects the difference in composite action offered by bonded or bolted connections. From the load-lateral displacement curves, evident lateral

deformation observed from MB specimens (see Fig. 10c and d) while limited lateral deformation from on AB specimens (lateral displacements less than 10 mm, see Fig. 10a and b). The differences in the load-bearing capacities of GFRP sandwich assemblies with these two types of connections are minor (within 5%).

6. Conclusions

This paper investigated the performance of GFRP sandwich assemblies in compression for column or wall applications. GFRP sandwich specimens were assembled by connecting two pultruded GFRP panels and two GFRP SHS using two approaches, i.e. adhesive bonding or mechanical bolting. The failure modes, load-bearing capacities, load-displacement curves and load-strain responses were obtained from experiments and compared with theoretical and FE modelling. The effects of different connection methods and the spacing between SHS sections were discussed. The following conclusions can be drawn from this study:

1. Adhesively bonded sandwich specimens (AB-1/2) experienced sudden debonding failure between the GFRP face sheets and inner SHS sections without global buckling in the experimental study. Mechanical bolted sandwich specimens (MB-1/2) exhibited evident lateral deformation and global buckling initiation. Progressive failures were found from the bolted sandwich specimens. Specimen MB-1 with a smaller spacing value of 96 mm between two inner SHS sections showed end crushing and web-flange junction separation at the end, after the obvious lateral deformation without local buckling of the GFRP face sheets. Specimen MB-2 with a larger spacing of 246 mm exhibited clear local buckling of face sheet wrinkling during the loading and it ultimately failed by the junction separation of SHS columns at the middle height of the specimen.

2. Load and displacement curves showed slightly higher axial stiffness of AB specimens than the MB specimens with the same section width. This may be due to the different degrees of composite action between the adhesive bonding and mechanical bolting and difference in the effective widths between two GFRP SHSs. Adhesive bonding provided full composite action between the GFRP face sheets and inner SHS sections; while mechanical bolting is associated with partial composite action. FE results on the load-axial displacement curves show good agreements with experimental results for both AB and MB specimens before failure. Load and lateral displacement curves of MB specimens showed more obvious lateral deformation than AB specimens. This also indicates global buckling initiated on MB specimens while not on AB specimens. Load-strain responses evidenced local buckling occurred on the GFRP face sheets of specimens AB-2 and MB-2.

3. It can be therefore identified that the spacing between the two SHS sections play an important role on the local buckling of the GFRP face sheets. Specimens AB-1 and MB-1 with a smaller spacing value of 96 mm did not exhibit local buckling on the face sheets while the local buckling was clearly found from specimens AB-2 and MB-2 with a larger spacing between the two inner SHS sections. Analytical results based on orthotropic plate theory was able to estimate the local buckling stress for the face sheets with satisfactory agreement with the experimental results.

The results from this study may demonstrated the compressive performance of the developed GFRP sandwich structures for potential column and wall applications by assembly of GFRP flat panels as face sheets and SHS as core sections. Different connection methods such as adhesive bonding and mechanical bolting and spacing values between core SHS sections as major design parameters may result in different failure modes, composite action degrees and load-bearing capacities.

Acknowledgements

References

[1] H.G. Allen, Analysis and Design of Structural Sandwich Panels, Pergamon Press, 1969.

[2] I.M. Daniel, J.L. Abot, Fabrication, testing and analysis of composite sandwich beams, Compos. Sci. Technol. 60 (2000) 2455–2463.

[3] K. Mallick P, Fiber-Reinforced Composites: Materials, Manufacturing, and Design, CRC Press, 2007.

[4] T. Keller, FRP sandwich structures in bridge and building construction, Proceedings of the Eighth International Conference on Fibre-Reinforced Polymer (FRP) Composites in Civil Engineering, 2016, pp. 23–28.

[5] A. Manalo, T. Aravinthan, A. Fam, B. Benmokrane, State-of-the-Art review on FRP sandwich systems for lightweight civil infrastructure, J. Compos. Constr. 21 (2017) 04016068.

[6] H. Fang, Y. Bai, W. Liu, Y. Qi, J. Wang, Connections and structural applications of fibre reinforced polymer composites for civil infrastructure in aggressive environments, Compos. Part B: Eng. 164 (2019) 129–143.

[7] W. Ferdous, Y. Bai, T. Ngo, A. Manalo, P. Mendis, New advancements, challenges and opportunities of multi-storey modular buildings – a state-of-the-art review, Eng. Struct. 183 (2019) 883–893.

[8] A. Fam, T. Sharaf, Flexural performance of sandwich panels comprising polyurethane core and GFRP skins and ribs of various configurations, Compos. Struct. 92 (2010) 2927–2935.

[9] H. Fang, H. Sun, W. Liu, L. Wang, Y. Bai, D. Hui, Mechanical performance of innovative GFRP-bamboo-wood sandwich beams: experimental and modelling investigation, Compos. Part B: Eng. 79 (2015) 182–196.

[10] A. McCracken, P. Sadeghian, Partial-composite behavior of sandwich beams composed of fiberglass facesheets and woven fabric core, Thin-Walled Struct. 131 (2018) 805–815.

[11] A.C. Manalo, T. Aravinthan, W. Karunasena, M.M. Islam, Flexural behaviour of structural fibre composite sandwich beams in flatwise and edgewise positions, Compos. Struct. 92 (2010) 984–995.

[12] B.D. Manshadi, A.P. Vassilopoulos, J. De Castro, T. Keller, Instability of thin-walled GFRP webs in cell-core sandwiches under combined bending and shear loads, Thin-Walled Struct. 53 (2012) 200–210.

[13] D. Zhu, H. Shi, H. Fang, W. Liu, Y. Qi, Y. Bai, Fiber reinforced composites sandwich panels with web reinforced wood core for building floor applications, Compos. Part B: Eng. 150 (2018) 196–211.

[14] S. Satasivam, Y. Bai, X.L. Zhao, Adhesively bonded modular GFRP web-flange sandwich for building floor construction, Compos. Struct. 111 (2014) 381–392.

[15] T. Sharaf, A. Fam, Analysis of large scale cladding sandwich panels composed of GFRP skins and ribs and polyurethane foam core, Thin-Walled Struct. 71 (2013) 91–101.

[16] S.Y. Shen, F.J. Masters, H.L. Upjohn, C.C. Ferraro, Mechanical resistance properties of FRP/polyol-isocyanate foam sandwich panels, Compos. Struct. 99 (2013) 419–432.

[17] T.K. Dey, I. Srivastava, R.P. Khandelwal, U.K. Sharma, A. Chakrabarti, Optimum design of FRP rib core bridge deck, Compos. B Eng. 45 (2013) 930–938.

[18] Z. Liu, P.K. Majumdar, T.E. Cousins, J.J. Lesko, Development and evaluation of an adhesively bonded panel-to-panel joint for a FRP bridge deck system, J. Compos. Constr. 12 (2008) 224–233.

[19] N.J. Lombardi, J. Liu, Glass fiber-reinforced polymer/steel hybrid honeycomb sandwich concept for bridge deck applications, Compos. Struct. 93 (2011) 1275–7283.

[20] T. Keller, J. Rothe, J. de Castro, M. Osei-Antwi, GFRP-balsa sandwich bridge deck: concept, design, and experimental validation, J. Compos. Constr. 18 (2014) 04013043.

[21] Y. Bai, T. Keller, Shear failure of pultruded fiber-reinforced polymer composites under axial compression, J. Compos. Constr. 13 (3) (2009) 234–242.

[22] I. Puente, A. Insausti, M. Azkune, Buckling of GFRP columns: an empirical approach to design, J. Compos. Constr. 10 (2006) 529–537.

[23] M.A. Mousa, N. Uddin, Global buckling of composite structural insulated wall panels, Mater. Des. 32 (2011) 766–772.

[24] M.A. Mousa, N. Uddin, Structural behavior and modeling of full-scale composite structural insulated wall panels, Eng. Struct. 41 (2012) 320–334.

[25] H. Mathieson, A. Fam, Numerical modeling and experimental validation of axially loaded slender sandwich panels with soft core and various rib configurations, Eng. Struct. 118 (2016) 195–209.

[26] H. Mathieson, A. Fam, Axial loading tests and simplified modeling of sandwich panels with GFRP skins and soft core at various slenderness ratios, J. Compos. Constr. 19 (2014) 1–13.

[27] H. Abdolpour, G. Escusa, J.M. Sena-Cruz, I.B. Valente, J.A.O. Barros, Axial performance of jointed sandwich wall panels, J. Compos. Constr. 21 (2017) 1–12.

[28] L. CoDyre, A. Fam, The effect of foam core density at various slenderness ratios on axial strength of sandwich panels with glass-FRP skins, Compos. B Eng. 106 (2016) 129–138.

[29] J. Tao, F. Li, D. Zhang, J. Liu, Z. Zhao, Manufacturing and mechanical performances of a novel foam core sandwich-walled hollow column reinforced by stiffeners, Thin-Walled Struct. 139 (2019) 1–8.

[30] L. Wang, W. Liu, Y. Fang, L. Wan, R. Huo, Axial crush behavior and energy absorption capability of foam-filled GFRP tubes manufactured through vacuum assisted resin infusion process, Thin-Walled Struct. 98 (2016) 263–273.

[31] T. Keller, J. de Castro, M. Schollmayer, Adhesively bonded and translucent glass fiber reinforced polymer sandwich girders, J. Compos. Constr. 8 (5) (2004) 461–470.

[32] T. Keller, T. Vallée, Adhesively bonded lap joints from pultruded GFRP profiles. Part II: joint strength prediction, Compos. B Eng. 36 (2005) 341–350.

[33] T. Keller, T. Vallée, Adhesively bonded lap joints from pultruded GFRP profiles. Part I: stress-strain analysis and failure modes, Compos. B Eng. 36 (2005) 331–340.

[34] L.C. Bank, Composites for Construction, Wiley, 2006.

[35] A.M. Girão Coelho, J.T. Mottram, A review of the behaviour and analysis of bolted connections and joints in pultruded fibre reinforced polymers, Mater. Des. 74 (2015) 86–107.

[36] M. Dakhel, T. Donchev, H. Hadavinia, Behaviour of connections for hybrid FRP/ steel shear walls, Thin-Walled Struct. 134 (2019) 52–60.

[37] J. Qureshi, J.T. Mottram, Behaviour of pultruded beam-to-column joints using steel web cleats, Thin-Walled Struct. 73 (2013) 48–56.

[38] C. Wu, Z. Zhang, Y. Bai, Connections of tubular GFRP wall studs to steel beams for building construction, Composites Part B: Engineering 95 (2016) 64–75.

[39] F.J. Luo, Y. Huang, X. He, Y. Qi, Y. Bai, Development of latticed structures with bolted steel sleeve and plate connection and hollow section GFRP members, Thin-Walled Struct. 137 (2019) 106–116.

[40] A. Mosallam, Design Guide for FRP Composite Connections, American Society of Civil Engineers (ASCE), 2011.

[41] The European Structural Polymeric Composites Group, Structural Design of Polymer Composites Eurocomp Design Code and Handbook vol. 35, (1996).

[42] B. Egan, C.T. McCarthy, M.A. McCarthy, R.M. Frizzell, Stress analysis of single-bolt, single-lap, countersunk composite joints with variable bolt-hole clearance, Compos. Struct. 94 (2012) 1038–1051.

[43] A.P.K. Joseph, P. Davidson, A.M. Waas, Progressive damage and failure analysis of single lap shear and double lap shear bolted joints, Compos. Appl. Sci. Manuf. 113 (2018) 264–274.

[44] J. Xiang, S. Zhao, D. Li, Y. Wu, An improved spring method for calculating the load distribution in multi-bolt composite joints, Compos. B Eng. 117 (2017) 1–8.

[45] L. Xie, Y. Bai, Y. Qi, H. Wang, Pultruded GFRP square hollow columns with bolted sleeve joints under eccentric compression, Composites Part B: Engineering 162 (2019) 274–282.

[46] S. Satasivam, Y. Bai, Mechanical performance of bolted modular GFRP composite sandwich structures using standard and blind bolts, Compos. Struct. 117 (2014) 59–70.

[47] A. Zhou, T. Keller, Joining techniques for fiber reinforced polymer composite bridge deck systems, Compos. Struct. 69 (2005) 336–345.

[48] T. Keller, H. Gürtler, Composite action and adhesive bond between fiber-reinforced polymer bridge decks and main girders, J. Compos. Constr. 9 (2005) 360–368.

[49] J.T. Coleman, J.J. Lesko, T.E. Cousins, A.B. Temeles, A. Zhou, Laboratory and field performance of cellular fiber-reinforced polymer composite bridge deck systems, J. Compos. Constr. 9 (2005) 458–467.

[50] L. Xie, Y. Bai, Y. Qi, C. Caprani, H. Wang, Effect of width-thickness ratio on capacity of pultruded square hollow polymer columns, Proc. Inst. Civ. Eng.: Struct. Build. 171 (2018) 842–854.

[51] ITW Performance Polymers, Plexus MA310, https://itwperformancepolymers. com/, (2018).

[52] Contact Technology Guide release 15.0. ANSYS Inc, Canonsburg PA; 2013.

[53] C.T. McCarthy, P.J. Gray, An analytical model for the prediction of load distribution in highly torqued multi-bolt composite joints, Compos. Struct. 93 (2011) 287–298.

[54] M. Pecce, E. Cosenza, Local buckling curves for the design of FRP profiles, Thin-Walled Struct. 37 (2000) 207–222.

[55] L. Shan, P. Qiao, Explicit local buckling analysis of rotationally restrained composite plates under uniaxial compression, Eng. Struct. 30 (2008) 126–140.

[56] D.C.T. Cardoso, K.A. Harries, E.D.M. Batista, Closed-form equations for compressive local buckling of pultruded thin-walled sections, Thin-Walled Struct. 79 (2014) 16–22.

[57] L. Kollár, Local buckling of fiber reinforced plastic composite structural members with open and closed cross sections, J. Struct. Eng. 129 (2003) 1503–1513.

[58] P. Qiao, Q. Chen, Post-local-buckling of fiber-reinforced plastic composite structural shapes using discrete plate analysis, Thin-Walled Struct. 84 (2014) 68–77.